Granular coefficient of restitution using coupled kinetic theory of granular flow and discrete element method

Jiang Xiaoxue [1], Wang Shuyan [2,*], Zhang Qinghong [1], Shao Baoli [2], Lu Huilin [1,*]

1 School of Energy Science and Engineering, Harbin Institute of Technology, Harbin, 150006, China

2 School of Petroleum Engineering, Northeast Petroleum University, Daqing, 163318, China

* Corresponding authors. E-mail addresses: wangshuyan@nepu.edu.cn (S. Wang), huilin@hit.edu.cn (H. Lu).

Abstract: The granular coefficient of restitution (CoR) is an empirical data of simulations using two-fluid model with kinetic theory of granular flow (KTGF). The CoR relates with binary inelastic collisions of discrete particles. In present study, an approach of coupled KTGF for Euler granular phase and discrete element method (DEM) for discrete particles is proposed. The granular CoR is computed from the binary collisions of discrete particles using DEM. The momentum transfer between the Euler gas phase and the discrete particles is calculated from the momentum transfer coefficient between the Euler gas phase and Euler granular phase. The viscous force of discrete particles of DEM is computed from the turbulent model of Euler gas phase. A correlation of granular CoR is proposed as a function of granular volume fractions. The simulated axial velocities of Euler granular phase and discrete particles are in agreement with experiments in a spout fluidized bed.

Keywords: Coefficient of restitution; Kinetic theory of granular flow; Discrete element method; Granular temperature; Fluidized bed.

1. Introduction

Gas-solid fluidized bed technology is applied in a variety of coal combustion, chemical and petroleum industrial applications because gas–solid mixing provides high heart and mass transfer rates in the bed. On the other hand, the design and optimization of fluidized bed is always a challenge because of the complex interactions of collisions of particles and hydrodynamic

interaction between gas phase and bed materials.[1-2] With increasing computational capacity, computational fluid dynamics (CFD) is critical to compute the hydrodynamics of gas-solid fluidized beds. [3-5]

The numerical simulations of the hydrodynamics of gas and bed materials of fluidized bed reactors can be described by the Euler-Euler two-fluid models (TFM). The volume-averaged continuity equation and the Navier-Stokes equations are used to describe the hydrodynamics of Euler gas phase and Euler granular phase. The granular stresses are modeled as a function of viscosity and pressure which are computed using kinetic theory of granular flow (KTGF). [6-11] The KTGF describes the dependence of the rheological properties owing to particle–particle binary collisions.[12-13] Savage and Jeffery considered a binary collection of spherical particles using elementary kinetic theory, and they recognize that in order to deduce explicit expressions for the stress tensor, it is necessary to determine the coefficient of restitution (CoR) although the KTGF allows the computation of the rheology of particles. The KTGF shows that the collisional energy dissipation increases with the decrease of granular CoR. The constitutive relations of particles indicate that the KTGF is almost free from empirical constants, and only the granular CoR has to be given. The discrete particles CoR is the ratio between the relative normal velocities before and after impact, and represents the loss of mechanical energy during binary collision. For an inelastic collision, the CoR is a real number between zero and one. Experimental data summarized by Johnson showed that for hard materials the CoR is nearly one for impact velocities less 0.1 m/s. [14] A constant CoR is used in KTGF as an adjustable parameter in numerical simulations of fluidized beds.[15-16] The influence of the constant CoR was studied in the range of 0.85-1.0 on the time-averaged volume fractions of the fluidized beds.[17] They found that the assumption of constant CoR of 1.0 results in the flow pattern without bubbles in the bed which is physically non-realistic. With

the decrease of CoR, the averaged volume fraction of particles decreases accordingly. The effect of constant CoR on gas volume fractions was studied in the range of 0.9 and 0.99 in 2D and 3D fluidized bed.[18] The influence of constant CoR on lateral distribution of solid volume fractions was found. A sensitivity analysis has assessed the influence of constant CoR on the solutions in the range of 0.9-0.99 of spouted beds.[19] The differences in velocity and volume fractions of particles were observed with the change of constant CoR in the spout and annulus of the bed. The effect of CoR on the dynamic behavior was analyzed in the range of 0.8-1.0 of fluidized bed.[20] Simulated results showed that the reduction of CoR tends to reduce the bed expansion. Precisely speaking, the constant CoR is not an adjustable parameter in the KTGF because it represents the physical kinetic energy loss during a collision.[21-22] Frequently, it is assumed that the CoR is a material constant which simplifies numerical simulations considerably. This assumption, however, disagrees with experiments.[14] As a result, the value of CoR affects the results significantly in numerical simulations using KTGF-based TFM in gas-solid fluidized beds. Hence, the constant CoR-based KTGF has to be compensated for the determination of CoR using additional models.

The flow behavior of the bed materials of the gas-solid fluidized bed is also modeled by means of Lagrangian approach to track the discrete particles in space and time.[23-24] In Euler-Lagrangian models (EL), the fluidizing gas phase is treated as a continuum by solving the time-averaged Navier-Stokes equations, while the discrete particles are described by the Lagrangian framework. The trajectories of discrete particles are calculated according to the motion equation and the collision model of discrete particles. The interactions of collisions between the discrete particle *i* and the discrete particle *j* was modeled using the direct simulation Monte Carlo (DSMC) method in gas-solid fluidized bed.[25-26] The collisional interactions are modeled according to collision probability of discrete particles. The discrete particles soft-sphere model and hard sphere model are

used in the deterministic detection of particle collisions. In hard-sphere models, the interaction of discrete particles is assumed to be instantaneous binary collisions.[27-28] In soft-sphere model, also known as discrete element method (DEM), the colliding discrete particles can overlap each other. The contact forces are determined through the displacement of discrete particles.[29-32] The multi-phase particle-in-cell (MP-PIC) model and the dense discrete phase model (DDPM) are used to simulate collisional interactions in gas-solid fluidized beds. The discrete particles are grouped into parcels and an empirical correlation of solid stress term is used to model collisions of discrete parcels in the MP-PIC model,[33-34] and the KTGF is used to calculate the collisional interactions between particles in the DDPM approach. Both MP-PIC and DDPM may limit the understanding of the mechanisms of collisional forces of discrete particles. On the other hand, the main feature of CFD-DEM is to provide detailed particle-scale information, which explains clearly the control mechanisms of the complicated flow behavior of the bed materials in gas-solid fluidized beds.[31] A detailed review on DEM is reviewed by Tsuji and Zhu et al. for numerical simulations of gas–solid fluidized beds without heat transfer and chemical reactions.[35-36]

Numerous amount of studies on the KTGF-based TFM and DEM applied for numerical simulations of fluidized beds show that these models are extensively used. The advantage of the KTGF-based TFM approach is that the transport equations for the gas-particle velocity correlation tensor, including the transport equation for the turbulent kinetic energy of the gas phase and granular phase are used to describe interfacial momentum transfer. The fluid-particle velocity covariance is determined using combined effect of particle collisions and gas turbulence. However, the limitation of the KTGF-based TFM is that a constant CoR is used to represent the interaction of binary collisions. When the volume fractions of particles are high, the binary collision mode might not be accurate, and the multiple collisions become dominant. The discrete character of the granular

phase, including collisions, cannot be identified. On the other hand, the advantage of the DEM that the Lagrangian trajectories of each discrete particle are computed and the inter–particle collisions are treated in a deterministic manner. However, the effect of the turbulent kinetic energy of the gas and granular phases and the gas-particle velocity covariance on motion of discrete particles cannot taken into account in formulations and numerical simulations, therefore reduces the quantitative ability of DEM simulations. A more general approach than the KTGF and DEM is needed, and this method can solve both multiple collisions for KTGF and discrete particles fluctuations of the discrete particles turbulent kinetic energy and gas-discrete particle velocity covariance for DEM.

In order to solve problems of granular CoR in KTGF-based TFM and turbulent motion of the continuous phase in CFD-DEM mentioned above, the hydrodynamics of bed materials of fluidized beds must be modeled by the KTGF for Euler granular phase and DEM for discrete particles. The granular CoR used in KTGF are obtained from the interactions of discrete particles using DEM. The gas viscous forces used in DEM for discrete particles are obtained from the Euler gas phase-Euler granular phase turbulent model, and the drag force of discrete particles used in DEM is calculated from the interphase momentum exchange between the Euler gas phase and the Euler granular phase. To achieve this, a model of coupled KTGF and DEM for Euler gas phase, Euler granular phase and Lagrangian discrete particles (CEEL) is proposed to describe the flow of bed materials using gas k_g-ε_g turbulent model, KTGF for Euler granular phase and DEM for discrete particles. The applicability of CEEL model is analyzed and verified in a comparative study of gas-solid single-spout fluidized bed with center gas jet. All fields of Euler gas phase, Euler granular phase and the motion of discrete particles are analyzed in the gas-solid fluidized bed. Finally, the distributions of CoR and granular temperatures are analyzed. The energy dissipations of discrete particles are calculated as a function of granular volume fractions in a gas-solid spout fluidized bed.

2. A model of Euler gas phase-Euler granular phase-Lagrangian discrete particles

It is assumed that the bed materials of the gas-particles fluidized bed consist of monodisperse particles with the diameter d_s and density ρ_s.

2.1. KTGF-based conservation equations of Euler granular phase

The mass and momentum conservation of the Euler granular phase without phase change and chemical reactions is:

$$\frac{\partial(\rho_s\alpha_s)}{\partial t}+\nabla\cdot(\rho_s\alpha_s\boldsymbol{u}_s)=0 \tag{1}$$

$$\frac{\partial}{\partial t}(\alpha_s\rho_s\boldsymbol{u}_s)+\nabla\cdot(\alpha_s\rho_s\boldsymbol{u}_s\boldsymbol{u}_s)=-\alpha_s\nabla p-\nabla p_s+\nabla\cdot\bar{\bar{\tau}}_s+\boldsymbol{f}_{gs}+\alpha_s\rho_s\boldsymbol{g} \tag{2}$$

where $\boldsymbol{u}_s$ and α_s and are the velocity and volume fraction of Euler granular phase. The granular pressure are expressed as follows[12]

$$p_s=\alpha_s\rho_s\theta+2\alpha_s^2\rho_s g_o(1+e_s)\theta \tag{3}$$

where e_s is the granular CoR. τ_s is the granular shear stresses according to shear viscosity and bulk viscosity, which are calculated as a function of granular temperature θ (i.e., θ=2<$\boldsymbol{CC}$>/3, $\boldsymbol{C}$ is the granular fluctuating velocity). The granular temperature of Euler granular phase has been used in order to solve transport equation in analogy with the kinetic theory of gases. The balance equation for the granular temperature is

$$\frac{3}{2}[\frac{\partial}{\partial t}(\alpha_s\rho_s\theta)+\nabla\cdot(\alpha_s\rho_s\boldsymbol{u}_s\theta)]=\nabla\cdot(k_s\nabla\theta)+(\nabla p_s\bar{\bar{\mathrm{I}}}+\bar{\bar{\tau}}_s):\nabla\boldsymbol{u}_s+\gamma_s-3\beta_{gs}\theta \tag{4}$$

where k_s and γ_s are the conductivity of fluctuating energy and collisional energy dissipation. They are listed in Table 1 as a function of granular CoR and temperature.

The partial slip boundary condition proposed by Johnson and Jackson is used to obtain

granular velocity and temperature at the wall.[21] The granular flux was equated to collisional dissipation through slip correction. The boundary conditions of Euler granular phase are

$$\boldsymbol{u}_{s,w} = -\frac{6\alpha_{s,max}}{\sqrt{3}\pi\phi g_o}\{\frac{10d_s\sqrt{\pi}}{96(1+e)g_o}[1+\frac{4}{5}(1+e_w)\alpha_s g_o]^2 + \frac{4}{5\sqrt{\pi}}\alpha_s d_s g_0(1+e_w)\}\frac{\partial \boldsymbol{u}_s}{\partial \boldsymbol{n}} \tag{5}$$

$$\theta_w = \frac{4\alpha_{s,max}}{\sqrt{3}\pi(1-e_w^2)\alpha_s\rho_s g_o\theta^{3/2}}[-k_s\theta\frac{\partial\theta}{\partial \boldsymbol{n}} + \frac{\sqrt{3}\pi\phi\rho_s\alpha_s u_s^2 g_o\theta^{3/2}}{6\alpha_{s,max}}] \tag{6}$$

where $\boldsymbol{n}$ is the normal component to the wall. e_w is the granular-wall coefficient of restitution. ϕ is the specularity coefficient which measures the average fraction of relative tangential momentum transferred from collisions against the walls, determined by empiricism. Thus, the character of the collisions between the granular phase and the wall can be look forward to affect the granular shear stress and the fluctuating energy flux as a function of granular-wall coefficient of restitution at the boundary.

2.2 Conservation equations for Lagrangian discrete particles

The motion of discrete particles is represented by linear velocity v_p and angular velocities ω_p through Newton's second law, expressed as follows[23]

$$m_i\frac{d\boldsymbol{v}_{pi}}{dt} = \sum_{j=1,i\neq j}^{N}\boldsymbol{f}_{c,ij} + \boldsymbol{f}_{d,i} + \boldsymbol{f}_{pf,i} + m_i\boldsymbol{g} \tag{7}$$

$$I_{pi}\frac{d\boldsymbol{\omega}_{pi}}{dt} = \sum_{j=1,i\neq j}^{N}\boldsymbol{T}_{p,ij} \tag{8}$$

where m and I_p are the mass and moment of inertia of the discrete particle. $\boldsymbol{T}_p$ is the torque due to the tangential components of the contact force. $\boldsymbol{f}_d$ is the drag force exerted by Euler gas phase on the discrete particle i in its residing computational cell. The contact force $\boldsymbol{f}_c$ is divided into the normal force $\boldsymbol{f}_n$ and tangential force $\boldsymbol{f}_t$, and they are determined as a function of spring stiffness coefficient k and dashpot damping coefficient η according to the normal displacement $\boldsymbol{\delta}_n$ and tangential

displacements $\boldsymbol{\delta}_t$ between the discrete particle i and j.[37]

$$\boldsymbol{f}_{nij} = (-k_n \boldsymbol{\delta}_{nij}^{3/2} - \eta_n \boldsymbol{v}_{rij} \cdot \boldsymbol{n}_{ij}) \boldsymbol{n}_{ij} \tag{9}$$

$$\boldsymbol{f}_{tij} = \begin{cases} -k_t \boldsymbol{\delta}_{tij} - \eta_t \boldsymbol{v}_{tij} & (|\boldsymbol{f}_{tij}| < \mu_f |\boldsymbol{f}_{nij}|) \\ -\mu_f |\boldsymbol{f}_{nij}| \dfrac{\boldsymbol{v}_{tij}}{|\boldsymbol{v}_{tij}|} & (|\boldsymbol{f}_{tij}| \quad \mu_f |\boldsymbol{f}_{nij}|) \end{cases} \tag{10}$$

The collisional interactions between the wall and the discrete particle are treated the same as particle–particle interactions as a function of wall Poisson ratio and wall elastic moduli except that the walls are assumed to be massive.

2.3 Conservation equations for Euler gas phase

The mass and momentum conservation equations for Euler gas phase are:[12]

$$\frac{\partial(\rho_g \alpha_g)}{\partial t} + \nabla \cdot (\rho_g \alpha_g \boldsymbol{u}_g) = 0 \tag{11}$$

$$\frac{\partial}{\partial t}(\alpha_g \rho_g \boldsymbol{u}_g) + \nabla \cdot (\alpha_g \rho_g \boldsymbol{u}_g \boldsymbol{u}_g) = -\alpha_g \nabla p + \nabla \cdot \bar{\tau}_g - \boldsymbol{f}_{gs} + \alpha_g \rho_g \boldsymbol{g} \tag{12}$$

where the expression of gas viscous stress tensor is as follows:

$$\bar{\tau}_g = \alpha_g (\mu_{gl} + \mu_{gt})[\nabla \boldsymbol{u}_g + (\nabla \boldsymbol{u}_g)^T] - \frac{2}{3} \alpha_g (\mu_{gl} + \mu_{gt}) \nabla \cdot \boldsymbol{u}_g \bar{I} \tag{13}$$

where the gas turbulent viscosity μ_{gt} is modeled by a k_g-ε_g turbulence model where k_g and ε_g are the gas turbulent kinetic energy and its dissipation rate.[38-39]

$$\frac{\partial}{\partial t}(\alpha_g \rho_g k_g) + \nabla \cdot (\alpha_g \rho_g \boldsymbol{u}_g k_g) = \nabla \cdot (\alpha_g \frac{\mu_{gt}}{\sigma_k} \nabla k_g) + \alpha_g G_k - \alpha_g \rho_g \varepsilon_g - k_{gs}(2k_g - \sqrt{2k_g}\sqrt{3\theta}) \tag{14}$$

$$\begin{aligned} &\frac{\partial}{\partial t}(\alpha_g \rho_g \varepsilon_g) + \nabla \cdot (\alpha_g \rho_g \boldsymbol{u}_g \varepsilon_g) = \\ &\nabla \cdot (\alpha_g \frac{\mu_{gt}}{\sigma_\varepsilon} \nabla \varepsilon_g) + \alpha_g \frac{\varepsilon_g}{k_g}(C_1 G_{kg} - C_2 \rho_g \varepsilon_g) - C_2 \frac{\varepsilon_g}{k_g} k_{gs}(2k_g - \sqrt{2k_g}\sqrt{3\theta}) \end{aligned} \tag{15}$$

where G_k is the turbulent kinetic energy arising from the mean velocity gradients. η_t is the ratio of Lagrangian integral time scale and the particle relaxation time. The empirical constants, C_1, C_2, C_μ, σ_k and σ_ε are 1.44, 1.92, 0.09, 1.0 and 1.3, respectively.

2.4. Momentum exchange among Euler gas and granular phases and discrete particles

The momentum exchange between the Euler gas phase and the Euler granular phase is accounted by means of a drag coefficient, which has a profound effect on the predictions using TFM. The appropriate choice of a drag coefficient is a key to successful fluidized bed simulations. Several drag models describing the momentum exchange between the granular phase and gas phase are derived by using the terminal velocity data for a single particle,[40] and pressure drop data from a dense packed bed.[12] The drag force is calculated by Huilin-Gidaspow model[41] according to the slip velocity between the gas phase and granular phase using a switch function φ.

$$\boldsymbol{f}_{gs} = \beta_{gs}(\boldsymbol{u}_g - \boldsymbol{u}_s) \tag{16}$$

$$\beta_{gs} = (1-\varphi)[150\frac{\alpha_s(1-\alpha_g)\mu_g}{\alpha_g d_s^2} + 1.75\frac{\alpha_s \rho_g \left|u_g - u_s\right|}{d_s}] + \varphi\frac{3}{4}C_d\frac{\alpha_s\alpha_g\rho_g}{d_s}\left|u_g - u_s\right|\alpha_g^{-2.65} \tag{17}$$

The drag force on the discrete particles is solved according to the momentum exchange coefficient β_{gs}.

$$\boldsymbol{f}_d = \frac{\beta_{gs}V_p}{\alpha_s}(\boldsymbol{u}_g - \boldsymbol{v}_p) \tag{18}$$

Thus, Both Eq. (16) and (18) couple the two drag forces, one is the discrete particle drag $\boldsymbol{f}_d$ used to solve the velocities of discrete particles, and the other is the interphase momentum transfer $\boldsymbol{f}_{gs}$ used in the momentum conservation equations of Euler gas phase and Euler granular phase.[42]

2.5. Coupling of CoR between Lagrangian discrete particle and Euler granular phase

The CoR between the discrete particle *i* and the discrete particle *j* measure the fraction of

kinetic energy recovered during a binary collision.[43-44] Several theoretical models for predicting the CoR are proposed according to the energy dissipation mechanism under different impact velocities. Johnson proposed a model including plastic dissipation during impact.[14] A similar model including an elastic effect during the collision was proposed in the elastic–plastic regime.[45] The expression for the CoR is expressed as a function of relative velocity v_{ij} of the discrete particle i and j, and E_i and G_i of elasticity moduli and Poisson's ratios of discrete particles.[45-46]

$$e_{ij} = \begin{cases} 0.998[2.078(1-\frac{1}{6}v_r^2)]^{0.5}\{v_r[v_r + 2\sqrt{1.2-0.2v_r^2}]^{-1}\}^{1/4} & v_r \le 1.0 \\ 0.998 & v_r > 1.0 \end{cases} \quad (19)$$

$$v_r = \frac{3.194}{v_{ij}}\{\frac{(1.61\sigma_{ys})^5 m_i m_j}{8(m_i+m_j)}(\frac{d_{si}d_{sj}}{d_{si}+d_{sj}})^3[\frac{E_j(1-G_i^2)+E_i(1-G_j^2)}{E_iE_j}]^4\}^{0.5} \quad (20)$$

where σ_{ys} is the material yield stress of discrete particles.

From Eq. (19), the CoR of discrete particles relate with relative velocity v_{ij} between the discrete particle i and discrete particle j, indicating the value of discrete particle CoR is not constant. The averaged discrete particles CoR is calculated in the grid

$$e_{sd} = \frac{1}{N}\sum_{j=1,i\neq j}^{N} e_{ij} \quad (21)$$

where N is the number of discrete particles in the grid.

For the CoR between the discrete particles and the wall, the value of CoR, e_{iw}, is also determined from Eq. (19) according to the relative velocity of discrete particle v_{pi} at the wall. The relative velocity between the discrete particle and the wall is

$$v_r = \frac{3.194}{128v_{\mathrm{pi}}}\{(1.61\sigma_{ys})^5 d_i^3 m_i[\frac{E_w(1-G_i^2)+E_i(1-G_w^2)}{E_iE_w}]^4\}^{0.5} \quad (22)$$

where E_w and G_w are the elasticity moduli and Poisson's ratios of the wall. The averaged CoR

between the discrete particles and the wall is calculated in the grid

$$e_{wd} = \frac{1}{N}\sum_{i=1}^{N} e_{iw} \tag{23}$$

From Eq. (21) and (23), we see that the averaged grid CoR of discrete particles is different from the discrete particles CoR because of the relative velocity difference between the discrete particles in the grid. The averaged grid CoR measures total energy dissipation during collisions of discrete particles. Therefore, the granular CoR is expressed as follows:

$$e_s = e_{sd} \tag{24}$$

$$e_w = e_{wd} \tag{25}$$

These equations give the relations between the granular CoR, ε_s and ε_w, used in the KTGF and the discrete particles CoR, e_{sd} and e_{wd}, determined from DEM. The coupled granular CoR and the discrete particles CoR keeps the same energy dissipation of collisions between the KTGF and the DEM simulations.

2.6 Time-splitting method coupled KTGF with DEM

In numerical simulations of discrete particles and Euler granular phase, the DEM is a one-way coupled method with the time step Δt_p of discrete particles, while the KTGF-based TFM is a four-way coupled method with the time step Δt. The discrete particles time step Δt_p is less than that of Euler granular phase Δt. Thus, the time-splitting method is used, and two steps are needed to solve CoR during the time step Δt. The time step Δt splits two interval parts. One is the sub-step Δt_a for the first half of the time step, and the other is the sub-step Δt_d for the rest time.[47-48] Thus, the time step is $\Delta t=\Delta t_a+\Delta t_d$ (where $\Delta t_a=0.5\Delta t$). First, the motion and trajectories of discrete particles are solved using e_s and e_w at the time step of Δt_p within the first fractional time step Δt_a. The positions and velocities of discrete particles are updated in the computational cell at the end Δt_a. The values

of $e_s(\Delta t_a)$ and $e_w(\Delta t_a)$ are determined according to the updated relative velocities of discrete particles. The values of updated e_s and e_w of Euler granular phase in the grid at the end time step Δt_a is

$$e_s(\Delta t) = ce_s(\Delta t_a) + (1-c)e_s(\Delta t_d) \tag{26}$$

$$e_w(\Delta t) = ce_w(\Delta t_a) + (1-c)e_w(\Delta t_d) \tag{27}$$

where $e_s(\Delta t_d)$ and $e_w(\Delta t_d)$ are the granular CoR and granular-wall CoR at the previous time interval step Δt_d. The weighting parameter c is 0.5. Then, the mass and momentum equations of Euler granular phase and Euler gas phase are solved according to $e_s(\Delta t)$ and $e_w(\Delta t)$. The above computing process will be repeated until the calculation reaches convergence at the end time step Δt_d. The two steps are connected together by the overall iteration procedure.

2.7 Numerical solver settings and procedures

Using MFIX code, the calculations of discrete particles CoR is implemented in the CALC_FORCE_DEM subroutine.[40] The time-splitting method is added in the DES_TIME_MARCH subroutine and the viscous forces of Euler gas phase are modified in the CALC_MU_g subroutine.[40] The calculation process can be seen in our previous paper.[42] The time step of Euler granular phase takes as 10^{-5} s to ensure the convergence of simulations. All simulations lasted for 25 s to obtain reliable time-average values and eliminate the influence of initial condition.

3. Comparison of experiments and simulations in a spout fluidized bed

The flow behavior of spout fluidized bed is measured using a particle image velocimetry and positron emission particle tracking.[49] The pseudo-3D spout fluidized bed simulated by Buijtenen et al. has a width, depth and height of 145 mm, 20 mm and 2500 mm with a spout jet at the center of

the distributor, as shown in Fig. 1.[49] The particles density and diameter of the bed materials are 2505 kg/m^3 and 3.0 mm with the minimum fluidization velocity of 1.9 m/s. Fluidizing gas is supplied though the spout jet with spouting velocity u_{sp} and the distributor with background velocity u_{bg}. The simulation parameters are shown in Table 2.

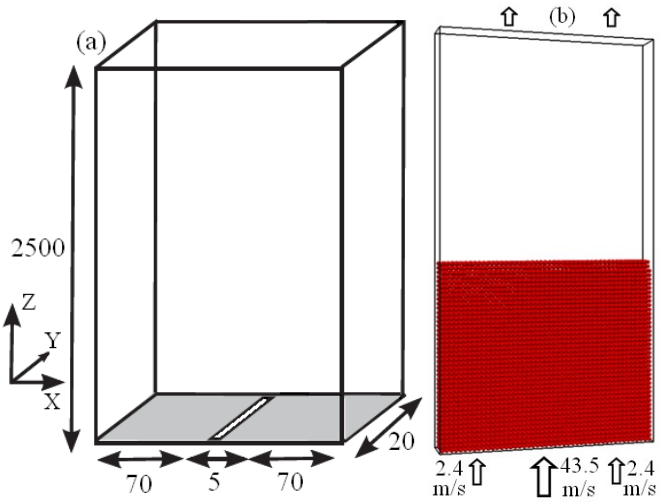

Fig. 1 Schematic overview of pseudo-3D single-spout fluidized bed of (a) Buijtenen et al. (2011) and (b) CEEL with dimensions in mm.

The instantaneous volume fraction contour of Euler gas phase, velocity vector of Euler granular phase and velocity color of discrete particles are shown in Fig. 2 at the inlet spouting velocity u_{sp} of 43.5 m/s and background velocity u_{bg} of 2.4 m/s. The colors of particles represent the velocity magnitude of discrete particles. The numerical simulations show that the dense annulus region near the walls and the dilute spout region at the center exist in the spout fluidized bed. The high inlet spout velocity with a low inlet background velocity makes a formation of spout channel in the bed center. This leads to the dilute spout channel with the upward flow of Euler granular phase and discrete particles in the center. However, the down-flow of Euler granular phase and discrete particles and the up-flow of Euler gas phase exist in the annular region. The circulation of Euler granular phase and discrete particles is formed in the bed. It is also found that the spout jet region is unstable, and moves the spout channel from side to side due to the competition between

the collisional interactions and the hydrodynamic interaction of the spout jet.

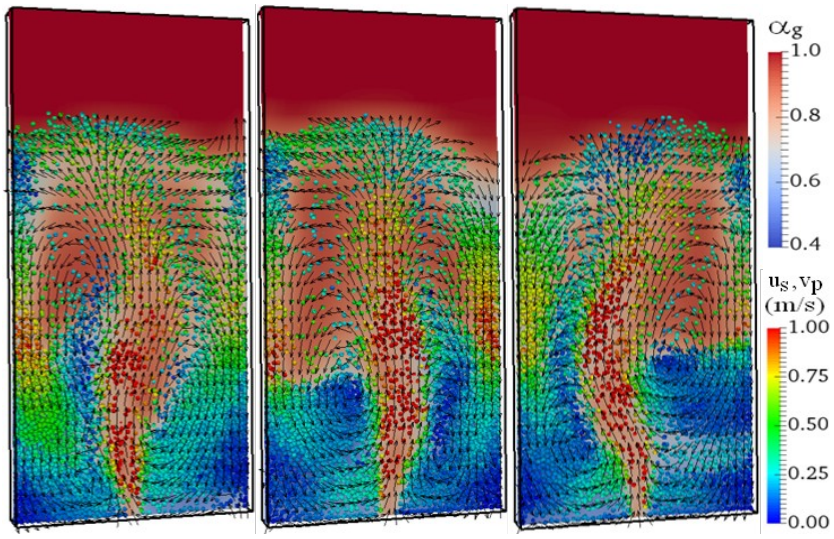

t=15s 20s 25s

Fig. 2 Instantaneous volume fraction contour of Euler gas phase, velocity vector of Euler granular phase and velocity color of discrete particles

The instantaneous velocity vector of Euler gas phase, granular temperature contour of Euler granular phase and rotational velocity color of discrete particles are shown in Fig. 3 in a spout fluidized bed. The colors of particles represent the rotational velocity magnitude of discrete particles in the bed. Gas ejects from the center jet of the distributor. The high rotational velocity of discrete particles is formed in the spout because the discrete particles flow from the annular region to the spout region. Numerical simulations further indicate that the granular temperatures of the Euler granular phase are high at the spout region and low at the annular region.

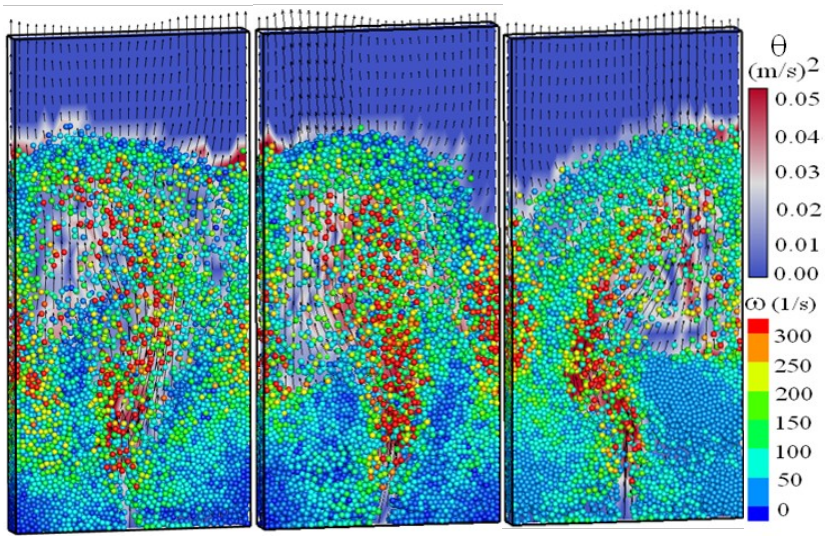

t=15s 20s 25s

Fig. 3 Instantaneous granular temperature contour of Euler granular phase, velocity vector of Euler gas phase and rotational velocity color of discrete particles

The averaged axial velocity of discrete particles is calculated according to simulated velocity of discrete particles in the grid. The simulated and measured axial velocities are shown in Fig. 4 along bed width. The simulated axial velocities of Euler granular phase and discrete particles match with experimental measurements. Both simulations and measurements show the axial velocities are positive at the spout region and negative at the annular region. However, the difference of axial velocities exists between simulations and experiments at two heights. The axial velocities of discrete particles are smaller than that of Euler granular phase at the dilute spout region. It is reverse in the annular region. The simulated axial velocities are larger than that of measurements at the interface between the spout region and the annular region, indicating that the numerical simulations over-predict the spout size in comparison with measurements in the spout fluidized bed.

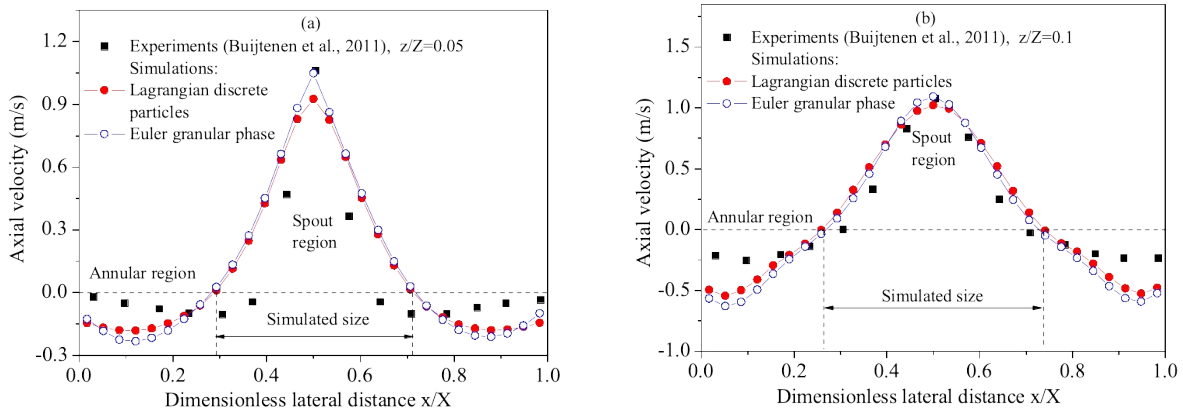

Fig. 4 Comparison of simulated and measured axial velocities at two bed heights

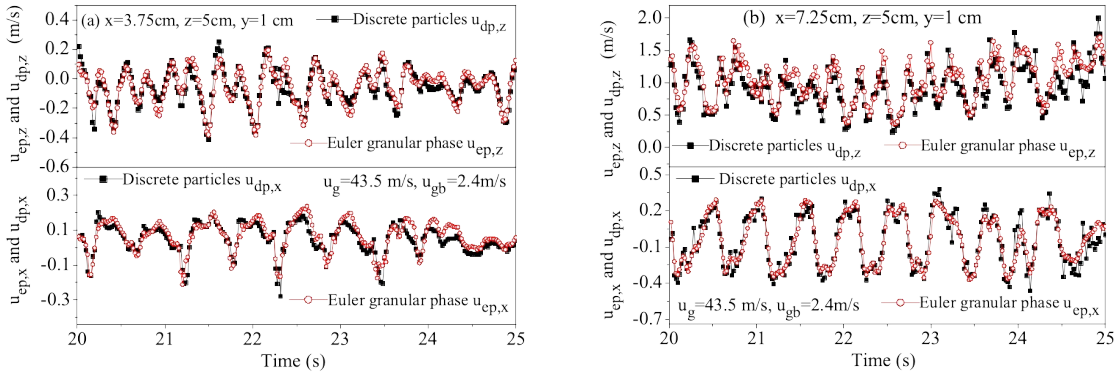

Fig. 5 Time series of axial and lateral velocities for Euler granular phase and discrete particles

The simulated instantaneous velocity components of Euler granular phase and Lagrangian discrete particles are shown in Fig. 5 at two heights. The large variations exist because of the lateral movement of gas jet. The formation of spout jet region occurs, and shows greatest spatial variations at the bottom of the bed.

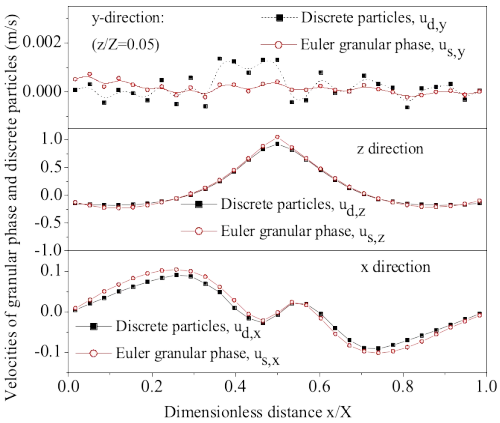

Fig. 6 Profile of velocity components of Euler granular phase and Lagrangian discrete particles

The time-averaged velocity components of Euler granular phase and Lagrangian discrete particles are shown in Fig. 6 at the dimensionless bed height of 0.05. The numerical simulations show that both velocity components are large along vertical *z* directions, and low along lateral *y* direction. The velocity components along *x* direction fall in between them. Both Euler granular phase and discrete particles move from the left and right walls to the center because the velocity component along *x* direction is positive at the left and negative at the right of the bed. It is further found that the velocity difference of granular phase and discrete particles are large along *y* direction, and the velocities along lateral direction are two orders of magnitude lower than that along vertical direction.

4. Distributions of granular and discrete particles CoRs

The granular CoR is computed from relative velocity during the collision between the discrete

particles *i* and *j*. The instantaneous granular CoRs and granular-wall CoRs are shown in Fig. 7 at two grids. The fluctuations of granular CoR attributes to the interactions of collisions of discrete particles due to the circulation of the bed materials upward flow in the center and downward flow near the wall. The time-averaged value shows that the low granular CoR is found at the center, and large granular CoR near the wall. The high gas jet velocity causes large energy dissipations due to the interactions of collisions of discrete particles, leading to a low granular CoR at the center. On the other hand, the instantaneous granular-wall CoRs are low in comparison with simulated granular CoR, indicating more energy dissipated between the Euler granular phase and the walls.

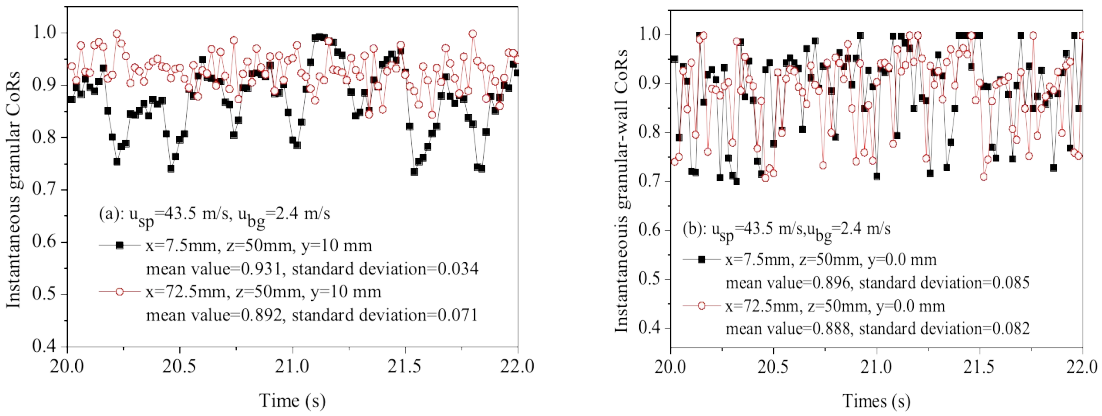

Fig. 7 Instantaneous computed granular CoRs and granular-wall CoRs at two grids

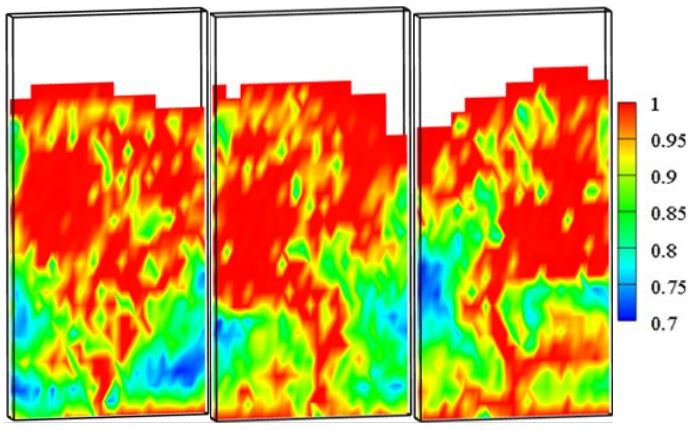

t=15s 20s 25s

Fig. 8 Instantaneous CoRs contours at three different times

Fig. 8 shows the instantaneous CoRs at three times. The instantaneous granular CoRs are large in the spout region because of low granular volume fraction. The collision frequency of discrete

particles is proportional to volume fractions of discrete particles. The larger the volume fraction is, the higher the collision frequency is, resulting in more energy dissipation with low granular volume fractions. Numerical simulations further illustrates that the instantaneous CoRs are low in the annulus because of the high granular volume fractions. The CoRs are large because the granular volume fraction is low at the bed surface. The mean CoR and standard deviation are calculated via statistical analysis. The mean granular CoR and granular-wall CoR are 0.97 and 0.89, indicating that the mean granular CoR is larger than granular-wall CoR in the bed. While the granular standard deviation is smaller than that of granular-wall CoR, indicating that more kinetic energy is dissipated though granular-wall interaction of collisions.

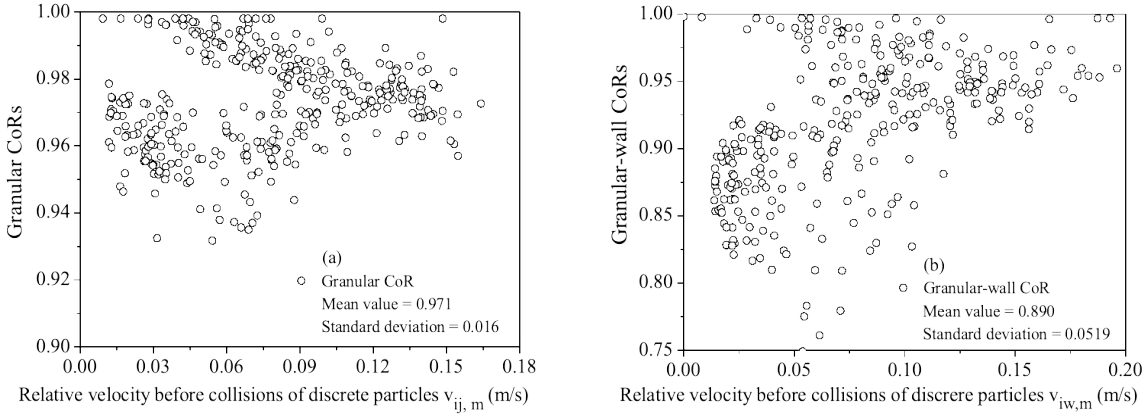

Fig. 9 Profile of granular CoRs and granular-wall CoRs as a function of relative velocity

From simulated instantaneous velocities of colliding discrete particles i and j, the relative velocity before collision v_{ij} is calculated. The averaged relative velocity before collision of discrete particles is

$$v_{ij,m} = \frac{1}{NM} \sum_{t=1}^{M} \sum_{i=1, i \neq j}^{N} v_{ij}(t) \tag{28}$$

where M is the number of over a given time period, and the N is the number of discrete particles in the grid. The distributions of averaged granular CoRs and granular-wall CoRs are shown in Fig. 9 as a function of relative velocity in the bed. Roughly, the granular CoRs decrease, and reach

minimum with the increase of relative velocity. After that they trend to constant at high relative velocity. Labous et al. and Falcon et al. found that the CoR varies $v_{ij}^{-1/4}$ when the impact velocity v_{ij} is large, and it is $1-e_s \propto v_{ij}^{1/5}$ when the impact velocity is low.[50-51] Simulated granular-wall CoRs indicate that there is considerable deviation that can be partially explained by the variations of volume fraction and velocity near the walls in the statistical analysis of collisions of discrete particles. The numerical simulations further indicate that the granular-wall CoRs decrease with the increase of relative velocity of discrete particles. The correlation for granular CoR and granular-wall are expressed as follows.

$$e_s = \frac{0.9996 + 50.662\alpha_s^2 - 787.668\alpha_s^4 + 4231.066\alpha_s^6}{1 + 52.596\alpha_s^2 - 804.905\alpha_s^4 + 4308.624\alpha_s^6 + 162.714\alpha_s^8} \tag{29}$$

$$e_w = \frac{0.9941 + 166.803\alpha_s^2 + 554.068\alpha_s^4 + 585.610\alpha_s^6 - 433.112\alpha_s^8 - 101.047\alpha_s^{10}}{1 + 193.871\alpha_s^2 + 758.09\alpha_s^4 - 115.524\alpha_s^6 + 458.983\alpha_s^8 + 115.647\alpha_s^{10}} \tag{30}$$

These correlations are corrected for the effect of multiple collisions at high granular volume fractions. As expected, both granular CoR and granular-wall CoR are high at low granular volume fractions. When the granular volume fractions increase, the probability of multiple collisions of discrete particles is expected to be relatively high, and the granular CoR and granular-wall CoR are reduced because the multiple collisions occur in the bed.

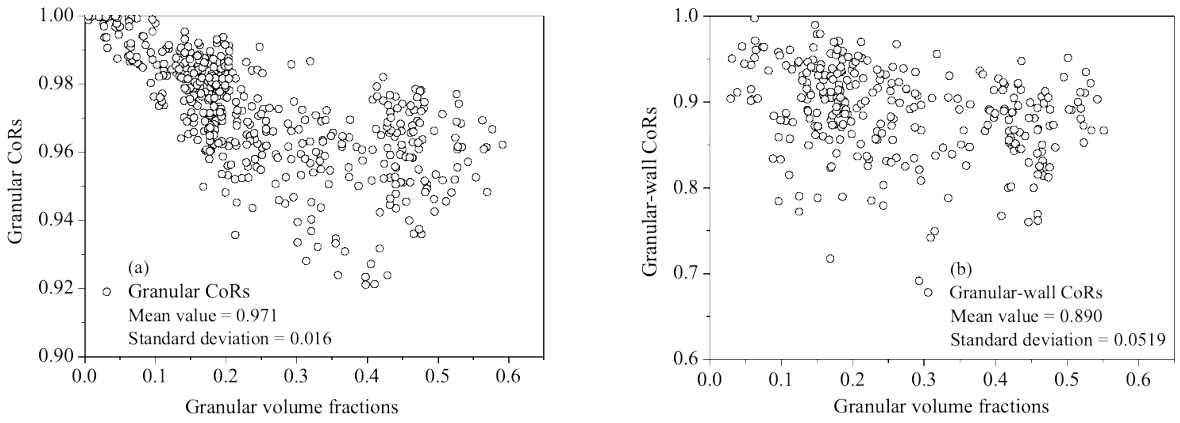

Fig. 10 Profile of granular CoRs and granular-wall CoRs as a function of granular volume fractions

Fig. 10 shows the distributions of granular CoRs and granular-wall CoRs as a function of granular volume fractions. Both granular CoR and granular-wall CoR decrease with the increase of granular volume fractions. The granular CoRs and granular-wall CoRs can change significantly at high granular volume fractions. With the increase of the number of discrete particles, the multiple collisions are dominant, indicating that the binary collision model is not be accurate in the prediction of energy dissipations of collisions, indicating the granular CoRs depend on the impact velocity in the normal direction and granular volume fractions.

5. Granular temperatures of Lagrangian discrete particles and Euler granular phase

The translational temperature components along x direction of Lagrangian discrete particles can be obtained by the instantaneous velocity v_{pi} and mean velocity v_m of discrete particles.

$$\theta_{px} = \frac{1}{n}\sum_{i=1}^{n}(v_{pi}(\boldsymbol{x},t) - v_m)(v_{pi}(\boldsymbol{x},t) - v_m) \tag{31}$$

It measures translational temperature component due to the random oscillation of discrete particles. The distribution of translational temperature component of discrete particles is shown in Fig. 11 at the center and near the wall. The translational temperature component of discrete particles varies with time and position in the spout and annular regions. The translational temperature component is

lower near the wall than that at the center. Numerical simulations further illustrate that the translational temperature components are larger along z axial direction than that along x and y lateral directions, meaning the velocity fluctuations of discrete particles are dominant along the direction of flow, and an anisotropic translational temperature component exists in the bed.

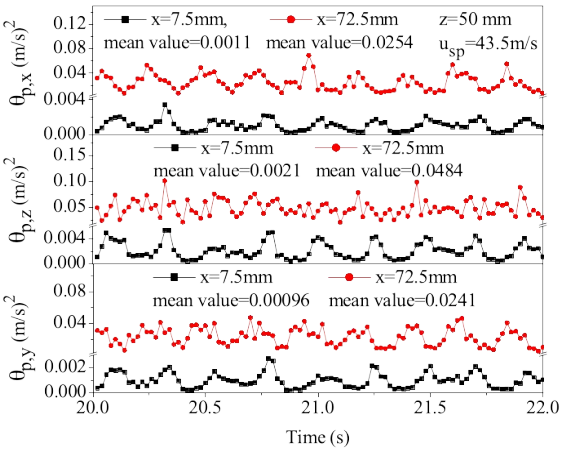

Fig. 11 Profile of instantaneous translational temperature components of discrete particles

The translational temperature θ_t of Lagrangian discrete particles is defined to be one-third the sum of the translational temperature components in the three directions.[12-13, 52] For motion of Lagrangian discrete particles, the collisions between slightly inelastic and slightly rough spheres are modeled using DEM, and additional transport parameter is given for the rotational kinetic energy. Similarly, the rotational temperature θ_r of Lagrangian discrete particles is defined as the average of the square of the rotational velocity components in the three directions.[53]

$$\theta_r = \frac{I_p}{3m}\sum_{k=1}^{3}[\frac{1}{n}\sum_{i=1}^{n}(\omega_{p,i}(\boldsymbol{x},t)-\omega_{im})(\omega_{p,i}(\boldsymbol{x},t)-\omega_{im})]_k \qquad (32)$$

where k is the direction of flow, and ω_{im} is the mean angular velocity of discrete particles.

The instantaneous rotational temperatures of Lagrangian discrete particles are shown in Fig. 12 at two computational cells. The high rotational temperatures at the center and low rotational temperature near the wall contributes the circulations of discrete particles upward flow in the center and downward flow near the walls. The rotation of discrete particles causes additional energy

dissipation.

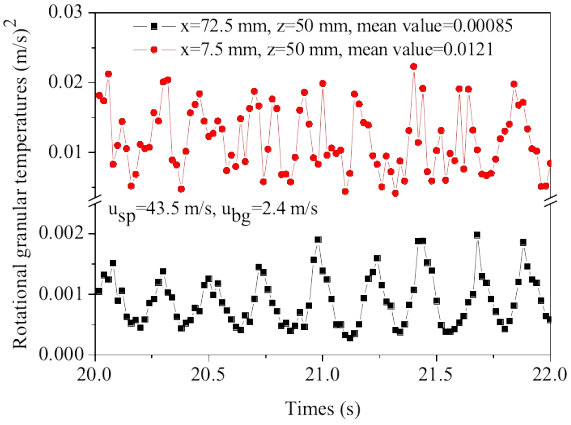

Fig. 12 Instantaneous rotational temperatures of discrete particles

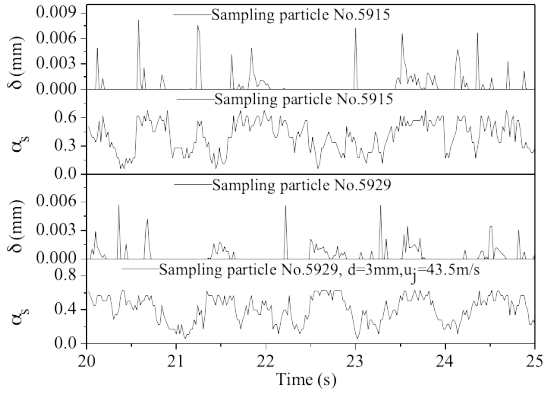

Fig. 13 Instantaneous of overlap of sampling discrete particles and granular volume fractions

From the trajectories and position of discrete particles, the overlap δ_i of the ith collision of discrete particles is determined. The instantaneous overlap δ_i of two sampling discrete particles is shown in Fig. 13 with the change of granular volume fractions. As the sampling particle passes through the grid, it will contact with other discrete particles with the grid. The higher the granular volume fraction is, the larger the overlap of sampling discrete particle is. The reverse trends are also observed, indicating the instantaneous overlap of the sampling discrete particle relate with the number of discrete particles of the grid.

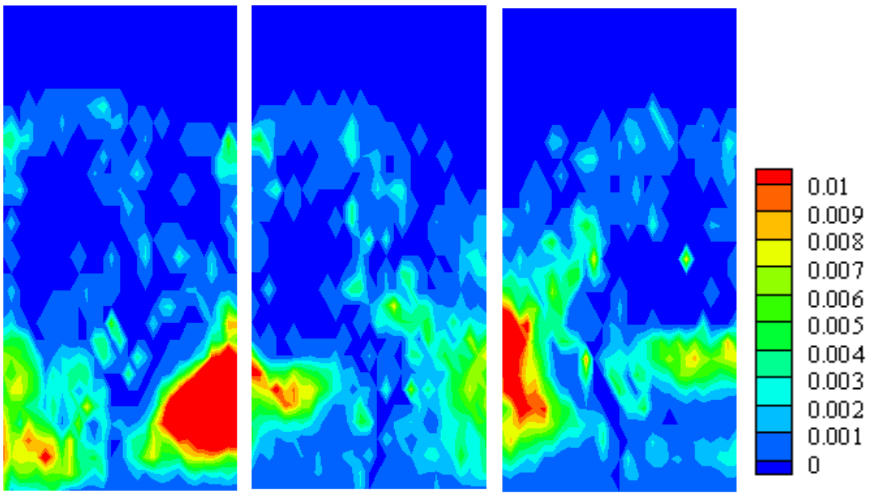

t=15s 20s 25s

Fig. 14 Instantaneous overlaps (mm) of discrete particles in the bed

The instantaneous overlaps of discrete particles are shown in Fig. 14 in the bed. The instantaneous overlaps are low at the spout region and near the bed surface. They are large in the annular region with high granular volume fractions. Simulated overlaps indicate that the interaction of collisions is dominant through multi-particle contacts in the annular region.

The contact forces exist at the contact between two contacting discrete particles, leading to the collision duration becomes comparable to the collision interval with the increase of granular volume fractions. Hence, the sustained multi-particle contacts prevail at high granular volume fractions. Similar to the definition of translational and rotational temperatures of discrete particles, the configurational temperature of discrete particles is defined as[53]

$$\theta_c = \frac{1}{3mN_c}\sum_{n=1}^{N_c} k_n \delta_i^2 \tag{33}$$

where N_c is the number of contacts in the grid. The configurational temperature θ_c represents fluctuation of overlaps, and measures the compaction capacity of discrete particles.[53] From Eq. (31), it can be seen clearly that the configurational temperature relates with the distance of the contact point from the center of the discrete particle i and particle j for impacting overlap. Therefore, the configurational temperature is calculated according to the configurations of discrete particles.

The distributions of configurational temperatures of Lagrangian discrete particles are shown in Fig. 15 in the bed. The configurational temperatures are low because of low collisions frequency at the low granular volume fractions. They increase and reach maximum at the granular volume fractions of 0.3. After that the configurational temperatures are reduced at high granular volume fractions. The mean configurational temperature is 0.0029 $(m/s)^2$ in the bed.

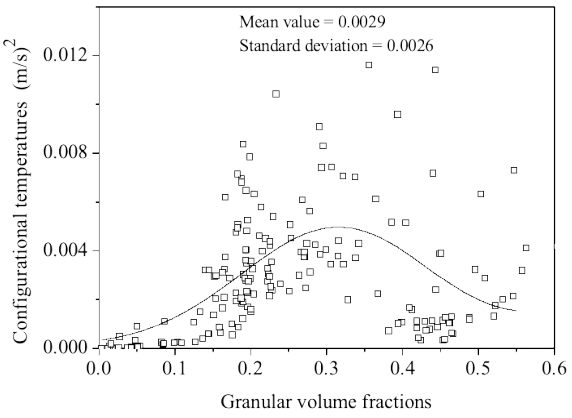

Fig. 15 Distributions of configurational temperatures of discrete particles

The translational and rotational temperatures represent the translational and rotational kinetic energy components of Lagrangian discrete particles due to the interactions of collisions. On the other hand, the interparticle contact will be dominant as the granular volume fraction increases. For the contact between two discrete particles, when the particles deform, the strain changes at the same time, resulting in the generation of contact force and deformation fluctuation kinetic energy component. Thus, the generalized granular temperature of Lagrangian discrete particles is the sum of three fluctuation kinetic energy contributions.

$$\theta_p = \theta_t + \theta_r + \theta_c \tag{34}$$

On the other hand, the granular temperature of Euler granular phase is predicted using transport equation of granular kinetic energy. The distributions of granular temperature and generalized granular temperatures of discrete particles are shown in Fig. 16 as a function of granular volume

fractions. The granular temperatures and generalized granular temperatures decrease as the granular volume fractions increase. The measured granular temperatures using a shot noise technique by Cody et al. were in the range from 0.0025 to 0.0063 $(m/s)^2$.[54] The measured granular temperature using a CCD camera by Jung et al. was in the range of 0.0021 to 0.0037 $(m/s)^2$ in a gas-solid fluidized bed.[52] The measured granular temperature using magnetic resonance was from 0.0105 to 0.0120 $(m/s)^2$ in gas-fluidized bed.[55] Present simulations show that the mean value of granular temperature of Euler granular phase and generalized granular temperatures of Lagrangian discrete particles are 0.0245 $(m/s)^2$ and 0.0162 $(m/s)^2$, respectively. It is further found that the generalized granular temperatures of Lagrangian discrete particles by means of DEM are the same as granular temperatures of Euler granular phase using KTGF when the granular volume fractions are larger than 0.2. However, the difference exists at the low granular volume fraction. The granular temperatures of Euler granular phase are larger than the generalized granular temperatures of Lagrangian discrete particles at the low granular volume fractions because the kinetic energy dissipation term of Euler granular phase in the granular temperature conservation equations is neglected. The rate of energy dissipation includes the dissipation due to the inelastic collisions of discrete particles and the dissipation due to the interaction with Euler gas phase per unit volume. The production due to Euler gas phase turbulence using the correlation proposed by Koch and Sangani showed that the fluctuating motion of discrete particles was depressed due to gas viscous damping.[56] The gas viscous dissipation plays a more dominant role at low granular volume fractions.

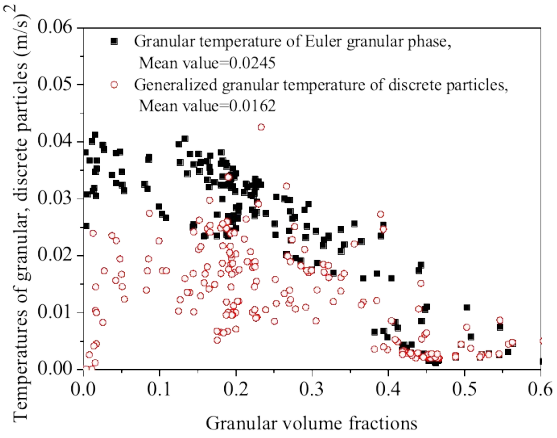

Fig. 16 Profile of granular temperatures of Euler granular phase and generalized granular temperature of Lagrangian discrete particles

6. Energy dissipations of Euler granular phase and Lagrangian discrete particles

From simulated velocity and displacements of discrete particles using DEM, the energy dissipations of collision of discrete particles are obtained. The total mechanical energy of Lagrangian discrete particles is the sum of the kinetic energy, potential energy and energy losses due to the interactions of drag forces and collisions of discrete particles. The elastic potential energy is stored as a result of deformation of discrete particles during collisions. The elastic potential energy could be accumulated or released due to the collisions between the discrete particles ΔE_{ep}, and between the discrete particles and the walls ΔE_{ew}. The collisional energy dissipation consists of the impact energy dissipation between the discrete particles ΔE_{ip} and between the discrete particles and the walls ΔE_{iw}, friction energy dissipation between discrete particles ΔE_{fp} and between the discrete particles and the walls ΔE_{fw}, and rolling energy dissipation between discrete particles ΔE_{rp} and between the discrete particles and the walls ΔE_{rw}.

$$\Delta E_p = (\Delta E_{ip} + \Delta E_{iw}) + (\Delta E_{fp} + \Delta E_{fw}) + (\Delta E_{rp} + \Delta E_{rw}) \tag{35}$$

The instantaneous energy dissipations of Lagrangian discrete particles are shown in Fig. 17 in the

bed. The instantaneous energy dissipations are oscillated due to the interactions of collisions and the hydrodynamic interactions through drag forces. In the impacting process of discrete particles, the kinetic energy is partially dissipated according to the motion of Newton laws. The first is impact energy loss due to the relative velocity between discrete particles and between the discrete particle and the walls. The second is friction energy dissipation due to the relative sliding between particles and between particles and walls. The last part is the dissipation of rolling energy resulting from rolling frictions on the contact area between discrete particles and between the discrete particles and the wall. The impact energy dissipation part between the discrete particles and between the discrete particles and the wall is largest, and the rolling energy dissipation is smallest. The friction energy dissipation falls in between them.

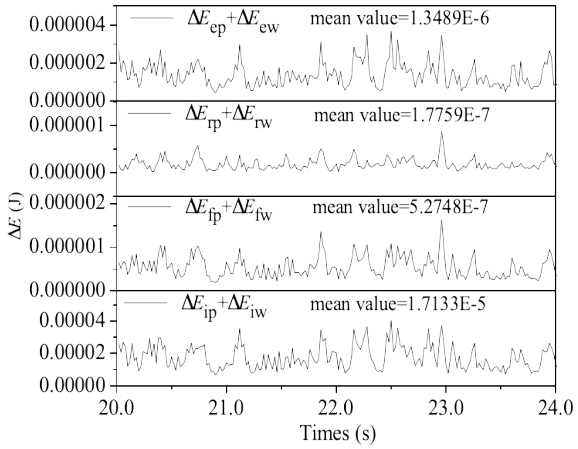

Fig. 17 Instantaneous energy dissipation portions of discrere particles

The energy dissipations of collisions of Euler granular phase are calculated using KTGF as a function of granular CoR. The energy dissipation due to inelastic collisions between the granular phase and the wall depends on granular-wall CoR.

$$\Delta E_S = \sum_{i=1}^{N} (\gamma_{s,i} \Delta V) \Delta t + \sum_{i=1}^{N_w} (\gamma_{w,i} \Delta V) \Delta t \tag{36}$$

The instantaneous collisional energy dissipations of Euler granular phase and Lagrangian discrete particles are shown in Fig. 18 in the bed. The collisional energy dissipations of Euler

granular phase have the same magnitude as the total energy dissipations of collisions of Lagrangian discrete particles. The mean values of collisional energy dissipations are 1.90×10^{-5} J and 1.77×10^{-5} J of Lagrangian discrete particles and Euler granular phase in the bed. The simulated results show that the macroscopic variation of energy dissipation of Euler granular phase using KTGF links to the microscopic information of Lagrangian discrete particles using DEM in the fluidized bed.

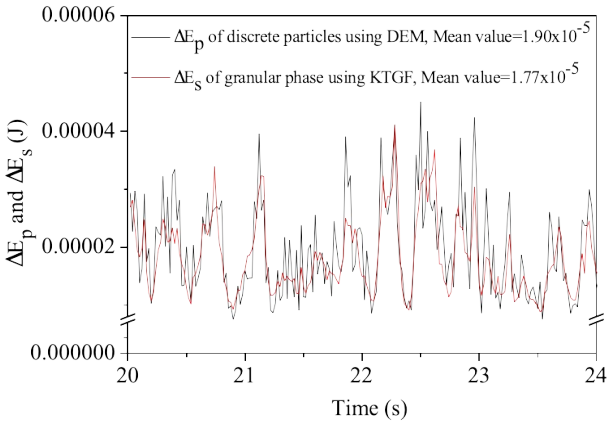

Fig. 18 Instantaneous collisional energy dissipations of Euler granular phase and Lagrangian discrete particles

7. Conclusion

This study presented a novel approach to determine granular CoR in numerical simulations using KTGF-based TFM of fluidized beds. The model coupled KTGF for Euler granular phase with DEM for Lagrangian discrete particles is proposed using a method coupled Euler gas phase, Euler granular phase and Lagrangian discrete particles (CEEL). The drag force on the discrete particles residing in the grid is determined from the momentum transfer of Euler gas phase-Euler granular phase. The viscous stresses acting on discrete particles are determined from Euler gas phase using k_g-ε_g turbulent model. The CoR of discrete particles is calculated using DEM. The granular CoR is calculated according to discrete particles CoR in the grid. The correlations of granular CoR and granular-wall CoR are proposed as a function of granular volume fractions, showing multiple

collisions contribution of discrete particles at high granular volume fractions.

The distributions of velocities and volume fractions of Euler granular phase and contact forces of discrete particles are predicted in the spout fluidized bed. The predicted velocities of Euler granular phase and discrete particles are in agreement with experimental measurements.

The translational and rotational temperatures of Lagrangian discrete particles are computed according to instantaneous translational and rotational velocities of discrete particles. The configurational temperature of Lagrangian discrete particles is calculated from instantaneous overlaps between discrete particles. The generalized granular temperature is proposed to measure the kinetic fluctuating energy of Lagrangian discrete particles. The simulated granular temperatures of Euler granular phase are close to generalized granular temperatures of Lagrangian discrete particles at high granular volume fractions.

The kinetic energy dissipations of Lagrangian discrete particles are analyzed according to normal and tangential spring forces using DEM. The impact energy dissipation is greater in comparison with rolling energy dissipation and friction energy dissipation in the bed. The collisional energy dissipation of Lagrangian discrete particles is approximately equal to the energy dissipation of Euler granular phase due to inelastic collisions in the bed.

ACKNOWLEDGMENTS

This study is partially supported by the National Natural Science Foundation of China under the grants Nos. 91752115 and 51776059.

Reference

[1] Grace JR, Avidan AA, Knowlton TM. Circulating fluidized beds. Blackie Academic & Professional. London, UK: Springer. 1997.

[2] Cocco R, Fullmer WD, Liu P, Hrenya C. CFD-DEM: Modeling the small to understand the large. *Chem Eng Prog*. 2017; 113: 38-45.

[3] Rao A, Jennifer SC, Hancock BC, Wassgren C. Numerical simulation of dilute turbulent gas-particle flow with turbulence modulation. *AIChE J*. 2012; 58: 1381-1396.

[4] Arastoopour H, Gidaspow D, Abbasi E. Computational transport phenomena of fluid-particle system. New York: Springer. 2016.

[5] Patel RG, Desjardins O, Kong B, Capecelatro J, Fox RO. Verification of Eulerian–Eulerian and Eulerian–Lagrangian simulations for turbulent fluid–particle flows. *AIChE J*. 2017; 63: 5396-5412.

[6] Lun CKK, Savage SB, Jeffrey DJ, Chepurniy N. Kinetic theories for granular flow: inelastic particles in curette flow and slightly inelastic particles in a general flow field. *J. Fluid Mech.* 1984; 140: 223-256.

[7] Ding J, Gidaspow D. A bubbling fluidization model using kinetic theory of granular flow. *AIChE J*. 1990; 36: 523-538.

[8] Hrenya CM, Sinclair JL. Effects of particle-phase turbulence in gas–solid flows. *AIChE J*. 1997; 43: 853–869.

[9] Arastoopour H. Numerical simulation and experimental analysis of gas-solid flow systems: 1999 Fluor-Daniel Plenary lecture. *Powder Technol*. 2001; 119: 59-67.

[10] Sundaresan S, Eaton J, Koch DL, Ottino JM. Appendix 2: Report of study group on disperse flow. *Int J Multiphase Flow*. 2003; 29: 1069–1087.

[11] Gidaspow D, Jung J, Singh RK. Hydrodynamics of fluidization using kinetic theory: an emerging paradigm 2002 Flour-Daniel lecture. *Powder Technol.* 2004; 148: 123-141.

[12] Gidaspow D. Multiphase flow and fluidization: Continuum and kinetic theory descriptions. New York: Academic Press. 1994.

[13] Huilin L. Kinetic theory for dense fluid-solid flow. Science Press. 2017.

[14] Johnson KL. Contact mechanics. Cambridge University Press. Cambridge, UK. 1985.

[15] Benyahia S, Syamlal M, O'Brien TJ. Evaluation of boundary conditions used to model dilute, turbulent gas/solids flows in a pipe. *Powder Technol*. 2005; 156: 62-72.

[16] Tingwen L, Benyahia S. Revisiting Johnson and Jackson boundary conditions for granular flows. *AIChE J*. 2012; 58: 2058-2068.

[17] Chanchal L, Himadri C, Pradip KC. Effect of coefficient of restitution in Euler–Euler CFD simulation of fluidized-bed hydrodynamics. *Particuology*. 2014; 15: 170–177.

[18] Shi H, Komrakova A, Nikrityuk P. Fluidized beds modeling: Validation of 2D and 3D simulations against experiments. *Pow*der Technol. 2019; 343:479–494.

[19] Cristina M, Filippo M, Laura O, Alfonso MF, Dominic VA, Elisabetta A. Sensitivity analysis and validation of a Two Fluid Method (TFM) model for a spouted bed. *Chem Eng Sci.* 2019; 207:39–53.

[20] Pascal F, Olivier S, Andrew I. 3D numerical simulation of a lab-scale pressurized dense fluidized bed focussing on the effect of the particle-particle restitution coefficient and particle–wall boundary conditions. *Chem Eng Sci.* 2016; 142:215–235.

[21] Johnson PC, Jackson R. Frictional-constitutive relations for granular materials, with application to plane shearing. *J Fluid Mech.* 1987; 176: 67–93.

[22] Gidaspow D, Huilin L. Equation of state and radial distribution functions of FCC particles in a CFB. *AIChE J*. 1998; 44: 279–293.

[23] Crowe C, Sommerfeld M, Tsuji Y. Multiphase flows with droplets and particles. CRC Press. Boca Raton. 1997.

[24] Fan LS, Zhu C. Principles of gas-solid flows. Cambridge University Press. 1998.

[25] Wang S, Liu H, Lu H, Liu W, Ding J, Li W. Flow behavior of clusters in a riser simulated by

direct simulation Monte Carlo method. *J. Chem. Eng.* 2005; 106:197-211.

[26] Huilin L, Zhiheng S, Jianmin D, Li X, Liu H. Numerical simulation of bubble and particles motions in a bubbling fluidized bed using direct simulation Monte-Carlo method. *Powder Technol*. 2006; 169:159-171.

[27] Hoomans BPB, Kuiper JAM, Briels WJ, Swaaij WV. Discrete particle simulation of bubble and slug formation in a two-dimensional gas-fluidized bed: a hard-sphere approach. *Chem Eng Sci*. 1996; 51: 99–118.

[28] Lu H, Wang S, Zhao Y, Yang L, Gidaspow D, Ding J. Prediction of particle motion in a two-dimensional bubbling fluidized bed using discrete hard-sphere model. *Chem Eng Sci*. 2005; 60: 3217–3231.

[29] Cundall PA, Strack ODL. A discrete numerical model for granular assemblies, *Geotechnique.* 1979; 29: 47–56.

[30] Tsuji Y, Kawaguchi T, Tanaka T. Discrete particle simulation of two-dimensional fluidized bed, *Powder Technol*. 1993; 77: 79–87.

[31] Xu BH, Yu AB. Numerical simulation of the gas–solid flow in a fluidized bed by combining discrete particle method with computational fluid dynamics. *Chem Eng Sci*. 1997; 52: 2785–2809.

[32] Kaneko Y, Shiojima T, Horio M. DEM simulation of fluidized beds for gas phase olefin polymerization. *Chem Eng Sci.* 1999; 54: 5809-5821.

[33] Andrews MJ, O'Rourke PJ. The multiphase particle-in-cell (MP-PIC) method for dense particulate flows. *Int J Multiphase Flow*. 1996; 22: 379-402.

[34] Snider D. An incompressible three dimensional multiphase particle-in-cell model for dense particle flows. *J Comput Phys.* 2001; 170:523-549.

[35] Tsuji Y. Multi-scale modeling of dense phase gas-particle flow. *Chem Eng Sci.* 2007; 62:

3410–3418.

[36] Zhu HP, Zhou ZY, Yang RY, Yu AB. Discrete particle simulation of particulate systems: theoretical developments. *Chem Eng Sci.* 2007; 62: 3378–3396.

[37] Zhou ZY, Kuang SB, Chu KW, Yu AB. Discrete particle simulation of particle-fluid flow: model formulations and their applicability. *J Fluid Mech.* 2010; 661: 482-510.

[38] Simonin O. Continuum modeling of dispersed two-phase flows, combustion and turbulence in two-phase flows. Von Karman Institute of Fluid Dynamics Lecture Series. 1996; 1– 47.

[39] Cao J, Ahmadi G. Gas-particle two-phase turbulent flow in a vertical duct. *Int J Multiphase Flow*. 1995; 21: 1203-1228.

[40] Syamlal M, Rogers W, O'Brien TJ. MFIX documentation theory guide. DOE/METC-94/1004, NTIS/DE94000087. 1993.

[41] Fluent Inc. Fluent 6.2 User's Guide. Lebanon: Fluent Incorporated. 2005.

[42] Qinghong Z, Shuyan W, Huilin L, Qiujing W, Ming T, Guodong L. Impact velocity-dependent restitution coefficient using a coupled Eulerian fluid phase-Eulerian solid phase-LDP phase model in gas-monodisperse particles internally circulating fluidized bed. *Int J Multiphase Flow*. 2018; 105: 142–158.

[43] Kuwabara G, Kono K. Restitution coefficient in a collision between two spheres. *Jpn J Appl Phys.* 1987; 26: 1230-1233.

[44] McNamara S, Falcon E. Simulations of dense granular gases without gravity with impact-velocity-dependent restitution coefficient. *Powder Technol*. 2008; 182: 232–240.

[45] Thornton C. Coefficient of restitution for collinear collisions of elastic perfectly plastic spheres. *J Appl Mech-T Asme.* 1997; 64: 383–386.

[46] Zhang Q, Wang S, Lu H, Liu G, Wang S, Zhao G. A coupled Eulerian fluid phase- Eulerian solids phase-LDP hybrid model applied to gas-solids bubbling fluidized beds. *Powder*

Technol. 2017; 315: 385–397.

[47] Pope SB. Computationally efficient implementation of combustion chemistry using in situ adaptive tabulation. *Combust Theor Model.* 1997; 1: 41-63.

[48] Geiser J, Hurso JL, Martinez E. New versions of iterative splitting methods for the momentum equation. *J Compt Appl Math.* 2017; 309: 359-370.

[49] Buijtenen MS, Dijk WJ, Deen NG, Kuipers JAM, Leadberater T, Parker DJ. Numerical and experimental study on multiple-spout fluidized bed. *Chem Eng Sci.* 2011; 66: 2368-2376.

[50] Labous L, Rosato AD, Dave RN. Measurements of collisional properties of spheres using high-speed video analysis. *Phys Rev E*. 1997; 56: 5717-5725.

[51] Falcon E, Laroche C, Fauve S, Coste S. Collision of a 1-D column of beads with a wall. *Eur Phys J B.* 1998; 5: 111–131.

[52] Jung J, Gidaspow D, Gamwo IK. Measurement of two kinds of granular temperatures, stresses, and dispersion in bubbling beds. *Ind Eng Chem Res*. 2005; 44: 1329–1341.

[53] Liyan S, Weiguo X, Huilin L, Guodong L, Qinghong Z, Qing T, Tianyu Z. Simulated configurational temperature of particles and a model of constitutive relations of rapid-intermediate-dense granular flow based on generalized granular temperature. *Int J Multiphase Flow*. 2015; 77: 1–18.

[54] Cody GD, Goldfarb DJ, Storch GV, Jr A, Norris AN. Particle granular temperature in gas fluidized beds. *Powder Technol*. 1996; 87: 211–232.

[55] Holland DJ, Muller CR, Dennis JS, Gladden LF, Sederman AJ. Spatially re-solved measurement of anisotropic granular temperature in gas-fluidized beds. *Powder Technol*. 2008; 182: 171–181.

[56] Koch DL, Sangani AS. Particle pressure and marginal stability limits for a homogeneous monodisperse gas-fluidized bed: kinetic theory and numerical simulations. *J. Fluid Mech.*

1999; 400: 229-263.